LETTERS
PUBLISHED ONLINE: 16 NOVEMBER 2015 | DOI: 10.1038/NPHYS3545
nature physics

All-optical generation of surface plasmons in graphene

T. J. Constant[1]*, S. M. Hornett[1], D. E. Chang[2] and E. Hendry[1]

Surface plasmons in graphene offer a compelling route to many useful photonic technologies[1–3]. As a plasmonic material, graphene offers several intriguing properties, such as excellent electro-optic tunability[4], crystalline stability, large optical nonlinearities[5] and extremely high electromagnetic field concentration[6]. As such, recent demonstrations of surface plasmon excitation in graphene using near-field scattering of infrared light[7,8] have received intense interest. Here we present an all-optical plasmon coupling scheme which takes advantage of the intrinsic nonlinear optical response of graphene. Free-space, visible light pulses are used to generate surface plasmons in a planar graphene sheet using difference frequency wave mixing to match both the wavevector and energy of the surface wave. By carefully controlling the phase matching conditions, we show that one can excite surface plasmons with a defined wavevector and direction across a large frequency range, with an estimated photon efficiency in our experiments approaching 10^{-5}.

Graphene has attracted significant interest recently as a unique optical material. In particular, it has been predicted and experimentally shown that graphene can support highly confined surface plasmons[1,9], with electrically tunable dispersion[7,8]. Despite these promising discoveries, the burgeoning field of graphene plasmonics has some serious obstacles to overcome if it is to progress from the proof-of-principle stage. Problems arise due to the small wavelength of the surface plasmons, two orders of magnitude smaller than light of the same frequency. This has led to the development of specialized measurement techniques, most of which use infrared light and geometries with scattering resonances[10–12] or near-field sources[7,8] to excite graphene surface plasmons. However, the far-infrared regime, in which graphene plasmons are predicted to have long lifetimes, lacks developed sources and detectors compared to the visible regime. Alternative approaches, such as the manipulation of surface acoustic waves to couple to the graphene surface plasmons[13,14], therefore hold promise.

Particularly desirable is the potential to excite a plasmon eigenstate with a singular energy, momentum and direction, vital for many future applications, including plasmonic circuits. In this respect, very recent progress has been made, with the development of carefully designed nanoantennas which can locally excite and direct surface plasmons in graphene[11]. Here, the combination of infrared source frequency and nanoantenna dimensions determine the frequency, wavevector and direction of the surface plasmons generated. In this letter, we investigate a competing approach that embodies many of these desirable aspects of directivity without requiring careful nanofabrication of antennas. This all-optical approach can access a distinctly broad frequency range, even down to the far infrared. We coherently excite surface plasmons using two visible frequency free-space beams via difference frequency generation (DFG), an effect which we monitor through changes in reflectance, and can tune the frequency and wavevector of the surface plasmon through careful adjustment of incident light sources. This potential to excite and detect plasmons purely with free-space optics, and at frequencies different from that of the plasmons themselves, has the potential to significantly expand the technological possibilities for graphene plasmonics.

The intrinsic nonlinear interactions of graphene with light are surprisingly large[5,15–18]. Moreover, large enhancements of nonlinear optical effects are predicted by the presence of highly confined plasmons in graphene[19,20]. It seems intuitive, then, to attempt the converse: to use the nonlinear interaction between optical fields to resonantly drive surface plasmons. Similar approaches have been demonstrated experimentally for thin metallic films[21,22], and have been recently proposed for graphene, with various coupling schemes proposed for the difference frequency mixing of infrared light in a graphene film[23] and in graphene-clad waveguide structures[23,24]. Similar in concept to that described in ref. 23, Fig. 1 shows our nonlinear coupling scheme illustrated on a dispersion diagram. By illuminating the graphene with two intense laser pulses with well-defined angles of incidence but different frequencies, labelled here f_{pump} and f_{probe}, one can phase match both the frequency and wavevector, k, of the surface plasmon. This wave mixing process is a second-order nonlinear effect, normally forbidden in centro-symmetric crystals[25], but possible in graphene because of the distinctively non-local, spatial character of the interaction[20]. The inset in Fig. 1 shows the experimental arrangement used (see Methods). The experiments are carried out in a non-collinear geometry, using two beams incident on the samples at angles θ_{pump} and θ_{probe} providing sufficient in-plane momentum to match to the surface plasmon, as illustrated in Fig. 1. We measure the differential reflection of the probe beam, defined as $\Delta R/R = (R - R_0)/R_0$, where R and R_0 are the reflections with and without the presence of the pump pulse, respectively. The polarization of both incoming beams is set in the plane of incidence (transverse magnetic polarized). To isolate the nonlinear reflection signal, we vary the temporal overlap of the two pulses.

For optical excitation, one expects optical nonlinearity arising due to saturable absorption caused by Pauli blocking of interband transitions[26]. A typical measurement of the temporal dynamics recorded for this process ($\lambda_{\mathrm{pump}} = 547\,\mathrm{nm}, \lambda_{\mathrm{probe}} = 615\,\mathrm{nm}$) is shown by the black curve in Fig. 2. Note that we normalize the signal by the pump fluence, Φ, to remove artefacts due to power variation[27]. The

[1]Electromagnetic Materials Group, Department of Physics, College of Engineering, Mathematics and Physical Sciences, University of Exeter, Exeter, Devon EX4 4QL, UK. [2]ICFO-Institut de Ciències Fotòniques, Mediterranean Technology Park, 08860 Castelldefels (Barcelona), Barcelona, Spain.
*e-mail: t.j.constant@ex.ac.uk

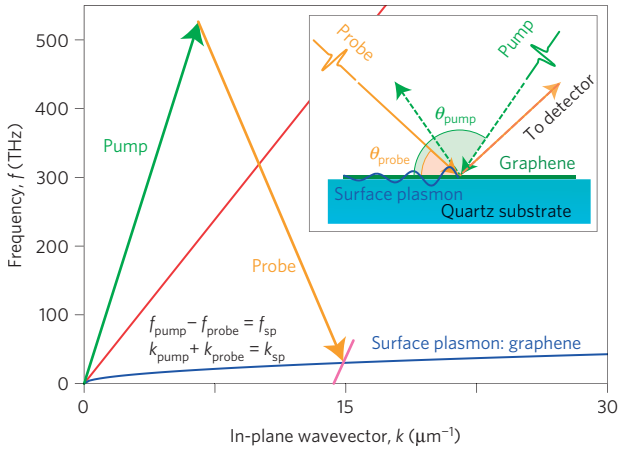

Figure 1 | The nonlinear coupling scheme illustrated on a dispersion diagram. The DFG of the pump (green arrow) and probe (orange arrow) allows access to wavevectors outside of the light line (red line). This permits phase matching to the surface plasmon modes in graphene (blue line). The pink line illustrates a region that can be interrogated by altering the pump wavelength from 615 to 545 nm with the probe wavelength fixed at 615 nm. (Inset) The experimental arrangement used to excite surface plasmons on graphene.

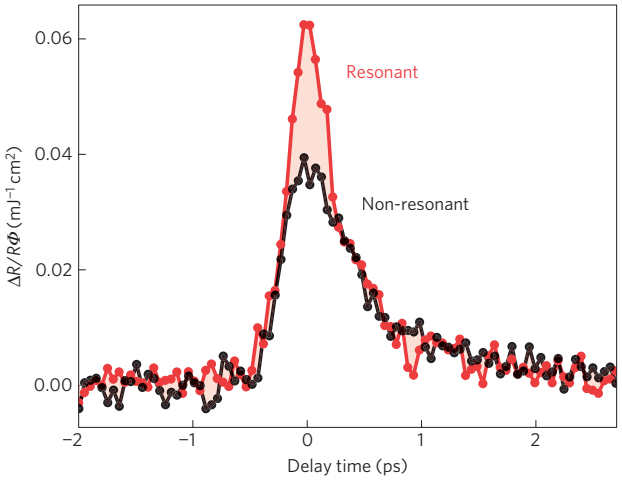

Figure 2 | Normalized differential reflection as a function of temporal overlap for the geometry $\theta_{pump} = 15°$, $\theta_{probe} = 125°$. At zero delay time, both the pump and probe pulses arrive simultaneously, leading to a nonlinear change in the probe reflection. Two curves are shown: The black curve labelled 'non-resonant' shows a typical time-asymmetric measurement when the difference frequency produced by the pump and probe (61.2 THz) does not coincide with a surface plasmon energy state. The red curve shows an additional fast symmetric contribution to the recorded reflection signal when the difference frequency matches the energy of a graphene surface plasmon (23.8 THz).

asymmetric line shape of the signal is due to the relaxation dynamics of the excited electrons cooling[27,28], with temporal broadening caused by the spatial overlap of the non-collinear beam spots.

For non-degenerate pump and probe beams, in addition to (incoherent) saturable absorption effects, one can expect (coherent) wave mixing signals. This coherent contribution to the probe reflection is expected to be significantly enhanced when the difference frequency field generated by the pump and probe matches that of the graphene surface plasmons. This is analogous to that of a stimulated Raman process, corresponding to a transfer of energy from pump to probe pulses[25] via the generation of surface plasmons. An example of the recorded temporal dynamics under such a resonant condition is presented in Fig. 2. Comparing the two curves in this figure, we see that the 'non-resonant' signal (that is, when one is not phase matching to plasmon excitation) gives rise to an asymmetric lineshape representative of carrier cooling dynamics. Under 'resonant' conditions (that is, when phase matching conditions are satisfied) we observe a fast additional contribution to the signal, giving rise to a more symmetric lineshape, as one would expect for a coherent signal. For certain experimental geometries and excitation fluences, signal enhancements of up to $\times 4$ are observed (see Supplementary Fig. 1). It should be noted that, depending on efficiencies, it may be possible to isolate the coherent signal using a heterodyne detection scheme[29], which could also allow detection of a plasmon in a different spatial position from where generated.

To observe the presence of the coherent signal, we vary the difference frequency from 0 to 60 THz to isolate any resonant, coherent conditions (see Methods). In this way, it is possible to interrogate a section of the surface plasmon dispersion, for example the region illustrated by the pink line in Fig. 1. By altering the experimental geometry, we investigate here three different regions of the dispersion diagram corresponding to ($\theta_{pump} = 55°, \theta_{probe} = 45°$), ($\theta_{pump} = 50°, \theta_{probe} = 70°$) and ($\theta_{pump} = 15°, \theta_{probe} = 125°$).

Figure 3 shows the results of these three measurement geometries, superimposed on the surface plasmon dispersion (black line). The dispersion was calculated according to the model outlined in ref. 30, with the SiO_2 substrate phonon frequencies as given and a Fermi energy of $E_f = 0.5$ eV. This Fermi energy is larger than the measured intrinsic doping of our graphene samples (see Methods for sample details), which we attribute to a significantly raised electron temperature expected under illumination by ultrafast pulses[31,32] (see Supplementary Information, Supplementary Fig. 2). Hybridization with the substrate phonons leads to four branches[30,33]. The overlaid colour plots are placed on the diagram so that the maximum differential reflection signal achieved in each delay-scan corresponds to the difference frequency and wavevector of the data set.

Near the regions defined by the surface plasmon dispersion in graphene, we observe clear enhancement in the differential reflection. The assignment of the spectral features to surface plasmon excitation is further supported by the polarization dependence of the signal (see Supplementary Fig. 3). The observation of these resonant features over the incoherent background is also strongly dependent on the magnitudes of both pump and probe intensities (see Supplementary Figs 1 and 2). For larger difference frequencies, up to 150 THz, we do not observe any further resonance features in our spectra (see Supplementary Fig. 4).

The lower branch of the plasmon dispersion relation gives rise to the largest mixing signals for the low-wavevector phase matching (set-ups a,b in Fig. 3), while the upper branches give rise to the largest signals for the high-wavevector (set-up c in Fig. 3) region. Although we observe clear resonance features in all three of these experimental geometries, we also observe a change in sign of the signal between the low- (Fig. 3a,b) and high-wavevector (Fig. 3c) regions. The absolute differential reflectivity signal size also increases with increasing wavevector.

To understand the origin of these coupling behaviours, we have developed a simple theoretical model that captures the salient features of this nonlinear reflection and generation of plasmons. We briefly summarize the model in the Methods (full details are presented in the Supplementary Information). In Fig. 4, we plot the modelled differential probe reflectance, normalized by fluence, for the simplified case of continuous plane-wave pump and probe beams. While this simple model ignores the non-equilibrium nature of the excitation, as observed in experiment, we show below that it is sufficient to describe some of the salient features of our

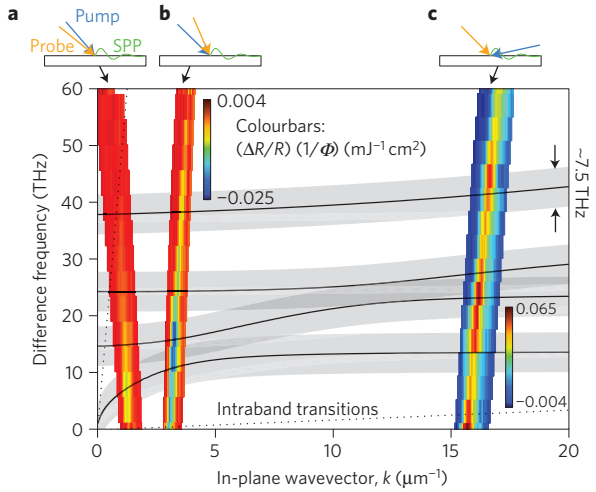

Figure 3 | Plots of normalized differential reflection for three different experimental geometries, superimposed on the graphene surface plasmon–phonon dispersion. The grey shading around the plasmon dispersion curves (black lines) indicates the expected spectral broadening of the signals (~7.5 THz) due to the finite bandwidth of ~100 fs-pulses. The set-ups used are depicted at the top of the figure with the angles used being $\theta_{pump} = 55°, \theta_{probe} = 45°$ (**a**), $\theta_{pump} = 50°, \theta_{probe} = 70°$ (**b**) and $\theta_{pump} = 15°, \theta_{probe} = 125°$ (**c**). The intraband transition threshold and light line (dotted lines) are labelled on the diagram. The colourbar for **a**,**b** is given at the top left and the colourbar for **c** is given at the bottom right.

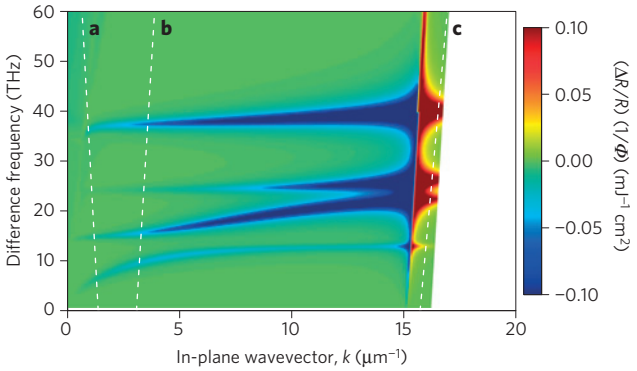

Figure 4 | Numerical solution for the normalized differential probe reflectance, calculated using the model outlined in the Supplementary Information. The white dotted lines **a**–**c** indicate the region of the dispersion relation probed by the experimental geometries shown in the equivalent parts of Fig. 3.

results. Similar to Fig. 3, the differential reflectance is plotted versus difference frequency and in-plane wavevector. It can be seen that the simulation qualitatively produces the main features of Fig. 3. In particular, the change in the sign of differential reflectance at the Brewster angle is clearly observed, as is the enhancement of the signal when the difference frequency and wavevector align with the plasmon dispersion relation.

The model also reproduces some of the main features arising from different coupling efficiencies to different bands (Fig. 4). Generally, the highest coupling efficiency occurs for the dispersion regions which are most 'plasmon-like' in origin (see also Supplementary Fig. 7). This is most obvious comparing the data in Figs 3c and 4c, where the coupling to the upper bands is much stronger than the lowest band in both model and experiment. For lower-wavevector cases, the coupling to the highest band is overestimated in the model compared to the experiment. This could possibly be caused by frequency-dependent losses in the graphene sheet unaccounted for in our simple model. The model also reproduces the increasing absolute signal strength with increasing wavevector observed in experiment, which is a consequence of both larger changes in the reflection coefficient for a corresponding change in absorption for higher angles, and due to spatial dispersion[20] in the signal. Indeed, it can be shown that the magnitude of enhancement is proportional to the square of the plasmon quality factor, Q^2 (see Supplementary Information), in agreement with predictions from ref. 23.

In addition to the surface plasmon resonance conditions, for the highest-wavevector region in Fig. 3c there is an additional resonant enhancement found in experiment at low frequencies (<3 THz) that is not reproduced in our model (Fig. 4c). The position of this peak lies within the expected region of intraband transitions in graphene, indicated by the dotted line in Fig. 3. This feature is also largely independent of polarization, unlike the enhancements we attribute to surface plasmon coupling (see Supplementary Fig. 3).

In principle, the reflection/transmission expressions obtained (see Methods, equation (1)) can be inverted to allow an experimental determination of the nonlinear conductivity $\sigma^{(2)}$, given transmission or reflection data. This is difficult in the present set-up, in part given the broad bandwidth of the pulses, uncertainty over some system parameters, and difficulty of investigating a large number of angles to quantify possible wavevector and frequency dependence of $\sigma^{(2)}$. However, as an estimate, we take the simplest possible model, in which the effective nonlinear susceptibility $\chi^{(2)}$ is independent of frequency and wavevector. This corresponds to a nonlinear conductivity function obeying $\sigma^{(2)}(\omega) = i|\sigma^{(2)}(\omega_{probe})|(\omega/\omega_{probe})$, where the value at the (fixed) probe frequency represents a single fitting parameter. We find that a value of $|\sigma^{(2)}(\omega_{probe})| \approx 2.4 \times 10^{-12}\,\mathrm{A\,m\,V^{-2}}$ produces the same peak signal as observed in Fig. 3b. It should be emphasized that this represents a rather conservative estimate of $\sigma^{(2)}(\omega)$. In particular, the mobility of $\mu \approx 2{,}000\,\mathrm{cm^2\,V^{-1}\,s^{-1}}$ corresponds to a plasmon linewidth of $\gamma = 2\pi \times 1.6\,\mathrm{THz}$ that is narrower than the measurement bandwidth, indicating that only a fraction of the pulse can efficiently excite plasmons. Reducing the measurement bandwidth could therefore give rise to greater coupling to the surface plasmons, while also reducing the effects of non-equilibrium carriers on the measurements. While a comparison to a bulk nonlinear crystal is not directly meaningful, it is nonetheless interesting to note that a bulk nonlinear crystal with the thickness $t \approx 0.3$ nm of a graphene layer would require a nonlinear susceptibility of $\chi^{(2)} \sim |\sigma^{(2)}(\omega_{probe})|/(\varepsilon_0 \omega_{probe} t) \sim 3 \times 10^{-7}\,\mathrm{m\,V^{-1}}$ to produce the equivalent in-plane nonlinear currents. This value is approximately three orders of magnitude larger than in GaAs.

Finally, from the inferred value of $\sigma^{(2)}$ and the input beam parameters, our model enables us to estimate the conversion efficiency η of pump photons to plasmons for our experimental pulse intensities (see Supplementary Information). We find a value of $\eta \approx 6 \times 10^{-6}$, while noting that the actual conversion could be significantly higher with narrow pulses, again as the estimated value of $\sigma^{(2)}$ does not account for the large pulse bandwidth. We note that this experimentally obtained value of η is of the same order as predicted in ref. 23, once adjusted for our experimental parameters.

To conclude, by carefully manipulating the phase matching conditions, we show that one can generate surface plasmons with a defined wavevector and an efficiency approaching 10^{-5} for the pulse intensities used. This efficiency by no means represents a fundamental limit, and we believe that it could in principle be pushed towards a 10^{-2} level with future adjustments, such as increasing the surface plasmon Q factor from ~5 to ~30 with lattice-matched hBN substrates[34], equalizing the intensities of the pump and probe beams (see Supplementary Fig. 1), or the use of narrower bandwidth pulses. Moreover, in principle, our approach could be

extended to higher or lower frequencies, regions that are generally hard to access using present approaches[2,35].

Methods

Methods and any associated references are available in the online version of the paper.

Received 30 April 2015; accepted 6 October 2015; published online 16 November 2015

References

1. Grigorenko, A. N., Polini, M. & Novoselov, K. S. Graphene plasmonics. *Nature Photon.* **6,** 749–758 (2012).
2. de Abajo, F. G. Graphene plasmonics: Challenges and opportunities. *ACS Photon.* **1,** 135–152 (2014).
3. Koppens, F. H. L., Chang, D. E. & de Abajo, F. J. Graphene plasmonics: A platform for strong light–matter interactions. *Nano Lett.* **11,** 3370–3377 (2011).
4. Craciun, M. F., Russo, S., Yamamoto, M. & Tarucha, S. Tuneable electronic properties in graphene. *Nano Today* **6,** 42–60 (2011).
5. Hendry, E., Hale, P. J., Moger, J., Savchenko, A. K. & Mikhailov, S. A. Coherent nonlinear optical response of graphene. *Phys. Rev. Lett.* **105,** 097401 (2010).
6. Brar, V. W., Jang, M. S., Sherrott, M., Lopez, J. J. & Atwater, H. A. Highly confined tunable mid-infrared plasmonics in graphene nanoresonators. *Nano Lett.* **13,** 2541–2547 (2013).
7. Fei, Z. *et al.* Gate-tuning of graphene plasmons revealed by infrared nano-imaging. *Nature* **487,** 82–85 (2012).
8. Chen, J. *et al.* Optical nano-imaging of gate-tunable graphene plasmons. *Nature* **487,** 77–81 (2012).
9. Bludov, Y. V., Ferreira, A., Peres, N. M. R. & Vasilevskiy, M. I. A primer on surface plasmon-polaritons in graphene. *Int. J. Mod. Phys. B* **27,** 1341001 (2013).
10. Gao, W., Shu, J., Qiu, C. & Xu, Q. Excitation of plasmonic waves in graphene by guided-mode resonances. *ACS Nano* **6,** 7806–7813 (2012).
11. Alonso-Gonzalez, P. *et al.* Controlling graphene plasmons with resonant metal antennas and spatial conductivity patterns. *Science* **344,** 1369–1373 (2014).
12. Gao, W. *et al.* Excitation and active control of propagating surface plasmon polaritons in graphene. *Nano Lett.* **13,** 3698–3702 (2013).
13. Farhat, M., Guenneau, S. & Bağcı, H. Exciting graphene surface plasmon polaritons through light and sound interplay. *Phys. Rev. Lett.* **111,** 237404 (2013).
14. Schiefele, J., Pedrós, J., Sols, F., Calle, F. & Guinea, F. Coupling light into graphene plasmons through surface acoustic waves. *Phys. Rev. Lett.* **111,** 237405 (2013).
15. Manzoni, M. T., Silveiro, I., de Abajo, F. J. G. & Chang, D. E. Second-order quantum nonlinear optical processes in single graphene nanostructures and arrays. *New J. Phys.* **17,** 083031 (2015).
16. Dean, J. J. & van Driel, H. M. Graphene and few-layer graphite probed by second-harmonic generation: Theory and experiment. *Phys. Rev. B* **82,** 125411 (2010).
17. Hong, S.-Y. *et al.* Optical third-harmonic generation in graphene. *Phys. Rev. X* **3,** 021014 (2013).
18. Gu, T. *et al.* Regenerative oscillation and four-wave mixing in graphene optoelectronics. *Nature Photon.* **6,** 554–559 (2012).
19. Gullans, M., Chang, D. E., Koppens, F. H. L., de Abajo, F. J. G. & Lukin, M. D. Single-photon nonlinear optics with graphene plasmons. *Phys. Rev. Lett.* **111,** 247401 (2013).
20. Mikhailov, S. A. Theory of the giant plasmon-enhanced second-harmonic generation in graphene and semiconductor two-dimensional electron systems. *Phys. Rev. B* **84,** 045432 (2011).
21. Renger, J., Quidant, R., van Hulst, N., Palomba, S. & Novotny, L. Free-space excitation of propagating surface plasmon polaritons by nonlinear four-wave mixing. *Phys. Rev. Lett.* **103,** 266802 (2009).
22. Palomba, S. & Novotny, L. Nonlinear excitation of surface plasmon polaritons by four-wave mixing. *Phys. Rev. Lett.* **101,** 056802 (2008).
23. Yao, X., Tokman, M. & Belyanin, A. Efficient nonlinear generation of THz plasmons in graphene and topological insulators. *Phys. Rev. Lett.* **112,** 055501 (2014).
24. Sun, Y., Qiao, G. & Sun, G. Direct generation of graphene plasmonic polaritons at THz frequencies via four wave mixing in the hybrid graphene sheets waveguides. *Opt. Express* **22,** 27880–27891 (2014).
25. Boyd, R. W. *Nonlinear Optics* 3rd edn (Elsevier, 2008).
26. Brida, D. *et al.* Ultrafast collinear scattering and carrier multiplication in graphene. *Nature Commun.* **4,** 1987 (2013).
27. Dawlaty, J. M., Shivaraman, S., Chandrashekhar, M., Rana, F. & Spencer, M. G. Measurement of ultrafast carrier dynamics in epitaxial graphene. *Appl. Phys. Lett.* **92,** 042116 (2008).
28. Hale, P. J., Hornett, S. M., Moger, J., Horsell, D. W. & Hendry, E. Hot phonon decay in supported and suspended exfoliated graphene. *Phys. Rev. B* **83,** 121404 (2011).
29. Borri, P. *et al.* Separation of coherent and incoherent nonlinearities in a heterodyne pump-probe experiment. *Opt. Express* **7,** 107–112 (2000).
30. Luxmoore, I. J. *et al.* Strong coupling in the far-infrared between graphene plasmons and the surface optical phonons of silicon dioxide. *ACS Photon.* **1,** 1151–1155 (2014).
31. Jensen, S. A. *et al.* Competing ultrafast energy relaxation pathways in photoexcited graphene. *Nano Lett.* **14,** 5839–5845 (2014).
32. Tielrooij, K. J. *et al.* Photoexcitation cascade and multiple hot carrier generation in graphene. *Nature Phys.* **9,** 248–252 (2013).
33. Yan, H. *et al.* Damping pathways of mid-infrared plasmons in graphene nanostructures. *Nature Photon.* **7,** 394–399 (2013).
34. Woessner, A. *et al.* Highly confined low-loss plasmons in graphene–boron nitride heterostructures. *Nature Mater.* **14,** 421–425 (2014).
35. Tonouchi, M. Cutting-edge terahertz technology. *Nature Photon.* **1,** 97–105 (2007).

Acknowledgements

This research has been supported by the European Commission (FP7-ICT-2013-613024-GRASP) and EPSRC fellowship (EP/K041215/1). D.E.C. also acknowledges support from Fundacio Privada Cellex Barcelona and the Ramon y Cajal programme. The authors would like to thank J. García de Abajo and M. Jablan for useful discussions, and N. Cole for technical assistance.

Author contributions

T.J.C. developed and carried out the experiments and data analysis, S.M.H. fabricated the samples and assisted with conceptual discussions, D.E.C. developed the theoretical model and fitting of experimental data, and E.H. designed the experiment and assisted in data analysis and interpretation. All authors contributed to writing of the paper.

Additional information

Supplementary information is available in the online version of the paper. Reprints and permissions information is available online at www.nature.com/reprints. Correspondence and requests for materials should be addressed to T.J.C.

Competing financial interests

The authors declare no competing financial interests.

Methods

Experimental arrangement. An identical pair of optical parametric amplifiers (OPAs), pumped by an amplified femtosecond laser system, generate the 100 fs-pulses at a repetition rate of 1 kHz. The wavelengths of the two OPAs are selected independently, and the beams are directed to the sample. The incident beams are weakly focused on the sample using 30 cm focal length lenses, giving rise to a very small uncertainty in angle ~0.017 rad, and a similarly negligible uncertainty for the in-plane wavevectors. Sets of half-wave plates and polarizers determine both the average power and polarization, with the polarization set such that the electric vector of the light is in the plane of incidence (transverse magnetic polarized). The pump pulse fluence, Φ, used is typically in the range $\Phi \sim 0.1-0.2\,\mathrm{mJ\,cm^{-2}}$, with a pump spot size on the sample of ~300 μm radius. This pump fluence is an order of magnitude less than the photo-modification threshold for graphene[36], and the probe fluence is typically two orders of magnitude smaller still.

To obtain difference frequencies from 0 to 60 THz, the pump wavelength is varied from 615 to 545 nm, with the probe wavelength set at 615 nm.

We record the differential reflection of the probe beam, defined as $\Delta R/R = (R - R_0)/R_0$, where R and R_0 are the reflections with and without the presence of the pump pulse, respectively. This differential reflection is recorded using a set of photo-balance diodes. To isolate the nonlinear reflection signal, we vary the temporal overlap of the two pulses using a motorized delay stage. Note that there is no appreciable signal from the quartz substrate (see Supplementary Fig. 8).

Sample preparation. Samples for our experiments are fabricated from commercially grown CVD graphene on copper foil (Graphene Supermarket). Transfer to quartz substrates was performed in house by means of a standard metal etching and float technique using ammonium persulphate to etch the copper and PMMA as a support structure. Combined resistance and Raman spectroscopy[37] give an estimated mobility of the samples of around $2{,}000\,\mathrm{cm^2\,V^{-1}\,s^{-1}}$ and a natural Fermi energy of ~300 meV. Raman imaging indicates that the graphene is nominally single layer, with ~80% coverage of the substrate.

Theoretical model. In general, equations for the electromagnetic boundary conditions at the air–graphene–substrate interface relate the wavevector- and frequency-dependent reflection and transmission coefficients $r(k,\omega), t(k,\omega)$ to the graphene current density $J(k,\omega)$. The current density, on the other hand, can be written in terms of the electric field using conductivity functions, which allows the equations to be solved in terms of fields alone. Nonlinear contributions imply that $J(k,\omega)$ depends on fields at other wavevectors and frequencies, which couple the various reflection and transmission coefficients together. For a second-order conductivity $\sigma^{(2)}$, we find that the probe transmission depends on the pump via

$$t_{\mathrm{probe}} = \frac{t^{(\mathrm{L})}_{\mathrm{probe}}}{1 - A\,(\sigma^{(2)})^2\,|t_{\mathrm{pump}}|^2\,I_{\mathrm{pump}}} \qquad (1)$$

with an analogous equation for the pump transmission (expressions for r are more involved but are directly related to t, see Supplementary Methods). Here $t^{(\mathrm{L})}_{\mathrm{probe}}$ is the linear transmission coefficient, A is a function of linear optical properties and beam angles with, for notational simplicity, dependencies on k,ω being implicit.

To model the differential reflectivity of the probe as shown in Fig. 4, the probe wavelength and pump angles are fixed at 615 nm and 50°, respectively, and the pump and probe intensities are chosen to be 10 and 0.1 $\mathrm{W\,\mu m^{-2}}$, to closely correspond to the configuration in Fig. 3b.

References

36. Alexeev, E., Moger, J. & Hendry, E. Photo-induced doping and strain in exfoliated graphene. *Appl. Phys. Lett.* **103,** 2011–2015 (2013).
37. Lee, J. E., Ahn, G., Shim, J., Lee, Y. S. & Ryu, S. Optical separation of mechanical strain from charge doping in graphene. *Nature Commun.* **3,** 1024 (2012).